Oceanic carbon capture through electrochemically induced in situ carbonate mineralization using bipolar membrane

Sharifian, R.; Boer, L.; Wagterveld, R. M.; Vermaas, D. A.

DOI
10.1016/j.cej.2022.135326

Publication date
2022

Document Version
Final published version

Published in
Chemical Engineering Journal

Chemical Engineering Journal 438 (2022) 135326

Contents lists available at ScienceDirect

Chemical Engineering Journal

journal homepage: www.elsevier.com/locate/cej

Oceanic carbon capture through electrochemically induced *in situ* carbonate mineralization using bipolar membrane

R. Sharifian [a,b], L. Boer [b], R.M. Wagterveld [b], D.A. Vermaas [a,*]

[a] Department of Chemical Engineering, Faculty of Applied Sciences, Delft University of Technology, The Netherlands
[b] Wetsus, European Centre of Excellence for Sustainable Water Technology, Leeuwarden, The Netherlands

A B S T R A C T

Bipolar membrane electrodialysis (BPMED) can provide a sustainable route to capture the oceanic-dissolved inorganic carbon (DIC) using an electrochemical pH-swing concept. Previous works demonstrated how gaseous CO_2 (through acidification) can be obtained from ocean water, and how carbonate minerals can be provided via *ex situ* alkalinization. In this work, we present, for the first time, the *in situ* mineralization via the alkalinization route using both real and synthetic seawater. An *in situ* pH-swing, inside of the BPMED cell, allows reducing the energy consumption of the oceanic-DIC capture. We demonstrate that, by accurately controlling the applied current density and cell residence time, the energy required for the process can be indeed lowered through facilitating an optimized pH in the cell (i.e., base-pH 9.6–10). Within this alkaline pH-window, we capture between 60% (for real seawater) up to 85% (for synthetic seawater) of the DIC from the feed, together with minor $Mg(OH)_2$ precipitates. The $CaCO_3$(s) production increases linearly with the applied current density, with a theoretical maximum extraction of 97 %. The energy consumption is dominated by the ohmic losses and BPM-overpotential. Through tuning the current density and flow rate, we optimised the energy consumption by applying a mild *in situ* pH-swing of ca. pH 3.2 – 9.75 (for real seawater). As a result, aragonite was extracted by using of 318 ± 29 kJ mol^{-1} $CaCO_3$(s) (i.e., ca. 0.88 kWh kg^{-1} $CaCO_3$(s)) from real seawater in a cell containing ten bipolar – cation exchange membrane cell pairs, which is less than half of the previously lowest energy consumption for carbonate mineralization from (synthetic) seawater.

1. Introduction

The damaging impacts of CO_2 on the climate encourages emission control and carbon capture to reduce the carbon footprint of all sectors [1]. In addition to capture from source points, CO_2(g) can be captured from its sinks including the atmosphere [2,3] and ocean [4,5], effectively addressing decentralized emissions. To ensure the carbon neutrality, this CO_2 capture should be able to be driven by renewable energy, which is most abundantly available as electricity. Thankfully, electrochemical methods can be used to achieve a circular carbon economy using (renewable) electricity [6] with no or minimal chemicals and at ambient temperature and pressure, as opposed to the conventional heat-driven CO_2 capture e.g., amine-based absorption or calcium looping. Electrochemical capture can be done via e.g., organic redox [7], pH-swing (via e.g., bipolar membrane electrodialysis, electrolysis, capacitive deionization, H^+ (de)intercalation, and proton-coupled electron transfer (PCET) of organic molecules), high-temperature molten carbonate cells, and hybrid methods (including electrochemical CO_2 capture and conversion combinations and battery systems) [6].

In particular, electrochemical cells containing a bipolar membrane (BPM) has shown promise for CO_2 capture, thanks to their simplicity to make acids and bases for releasing inorganic carbon from the water, their small footprint, and facile upscaling [6]. The bipolar membrane generates acidic and alkaline pH on its sides (i.e., pH-swing), through the water dissociation reaction (WDR) upon application of an electrical field in the reverse bias mode [8]. This pH-swing leverages the carbonate equilibrium, making it suitable for direct air capture (DAC), oceanic capture, and even flue gas capture [6,9]. Upon the pH-swing, the dissolved CO_2 in an aqueous solution can be captured in its gaseous form (at acidic pH) or as mineral carbonate (at alkaline pH) [4,6].

Approximately 23 % of the global CO_2 emission ends up in the ocean [6], making oceanic CO_2 capture advantageous as it eliminates the use of any additional aqueous absorbent (e.g., alkaline and amines in direct air capture) by leveraging the vast atmosphere–ocean contact area. Extracting 1 Gton-CO_2 per year (~2.7 % of the total global CO_2 emission) from the ocean surface layer (i.e., the upper 50 m) requires processing only a fraction of 0.0005 of this layer's volume [4]. Furthermore, ocean decarbonization combined with desalination plants (e.g., reverse osmosis), as a pre-treatment step, can potentially decrease the chance of carbonate scaling in the plant by reducing the DIC concentration below

* Corresponding author.
E-mail address: d.a.vermaas@tudelft.nl (D.A. Vermaas).

https://doi.org/10.1016/j.cej.2022.135326

Available online 17 February 2022

calcium carbonate solubility product.

The product of oceanic capture can be CO_2(g) or solid carbonate minerals, depending on the operating pH [8]. Extracting CO_2 in the gaseous form (from the acidic stream, Fig. 1A) has been demonstrated [4,10], but requires the use of additional gas–liquid membrane contactors for CO_2(aq) to CO_2(g) exchange. Additionally, purification of the produced CO_2(g) is required before it can be considered as feedstock [5], while the challenges concerning gas transportation and storage arise, accordingly.

On the other hand, for extraction of solid carbonate minerals via alkalinization of ocean water, no membrane contractors are required (Fig. 1B). Although the acid-route is more straightforward as negative emission technology (using the alkaline product to allow capturing CO_2 from the atmosphere again), the "alkalinization-route" could act also as circular oceanic CO_2 capture technology when the acid is used for other purposes. Possible combinations are using the slightly acidic stream for desalination (where the acidification prevents scaling [11]) or concentrating the acid further for industrial purposes. Returning only the alkaline, decarbonized stream, which has a pH between 9 and 10, brings net alkalinization to the ocean and allows further extraction of CO_2 from the atmosphere. A potential advantage of this "alkalinization-route" is that calcium carbonate is easy to transport, use, and store, and has a global market size of ~ 116 million ton $CaCO_3$ (i.e., ~ USD 43 billion in 2020, with annual growth rate of ~ 2.8 % [12]). Calcium carbonate applications include the paper industry (>50 % of the market [12], where it is used as filler), coating, plastics, paints, adhesive/sealants, rubber, cement and construction materials [13–15].

BPMED based oceanic-CO_2 capture through the alkalinization-route has been performed *ex situ* using synthetic seawater, where concentrated NaOH is first produced (from pure NaCl in BPMED) and then is gradually added to external storage tanks containing seawater, enabling the desired alkaline pH for carbonate mineralization [4]. Alternatively, during an *in situ* process, seawater is pumped directly into the electrochemical cell [16]. The *in situ* capture can eliminate the step of NaCl purification from the seawater, and avoids the necessity of making highly concentrated acid and base (i.e., large pH-swing), making the process more energy effective [17]. In fact, a mild pH-swing in the range of ~ pH 4–10 is adequate for CO_2 capture [18]. In addition, such mild pH-swing can preserve the lifetime and permselectivity of charged membranes better than a harsher pH-swing. However, although an *in situ* process might require less energy, it increases the chance of fouling within the cell.

In this work, we study the feasibility of the *in situ* bipolar membrane electrodialysis (BPMED) for capturing oceanic-dissolved inorganic carbon (DIC) as carbonate minerals via alkalinization route. Special attention is given to minimizing the electrical energy consumption of the process. First, the thermodynamic optimum alkaline pH-window for the capture and the minimum electrical energy required for the pH-swing is simulated using Visual MINTEQ 3.1. Subsequently, using a six-compartment cell with a single BPM, the effect of the (local) pH on the carbonate mineralization and membrane fouling is demonstrated. We perform experiments using both synthetic seawater and real seawater (from Wadden Sea in the Netherlands). Finally, we validated the concept in an upscaled BPMED cell, containing 10 bipolar – cation exchange membrane (BPM-CEM) cell pairs, providing insight towards industrialization of the carbon capture from seawater via mineralization.

2. Theory

2.1. Effect of pH-swing on the carbonate equilibrium

The atmospheric CO_2(g) is in equilibrium with the dissolved inorganic carbon (DIC) species in the ocean [19–23]. Oceanic-DIC has a concentration of ~ 2.3 – 2.5 mmol L^{-1}, and includes CO_2(aq)/ H_2CO_3, HCO_3^-, and CO_3^{2-} containing species [19]. At the typical surface seawater of pH ~ 8.2, these species contributions are 0.5 %, 89 %, and 10.5 %, respectively. Furthermore, calcium (and magnesium) ions are abundant in the ocean with concentrations ~ 4x (and ~ 20x) times higher than that of DIC, respectively [23]. Upon ocean alkalinization, the carbonate equilibrium shifts from the bicarbonate to carbonate ion [23,24]:

$$CO_2(aq) + OH^-(aq) \leftrightarrow HCO_3^-(aq) \quad (1)$$

$$HCO_3^-(aq) + OH^-(aq) \leftrightarrow H_2O + CO_3^{2-}(aq) \quad (2)$$

$$Ca^{2+}(aq) + CO_3^{2-}(aq) \leftrightarrow^{K_{sp}} CaCO_3(s) \quad (3)$$

Theoretically, >97 % of the DIC can be extracted in the form of ~ 2.13 mM CO_2 (g) when bringing the seawater pH to 4.5, or in the form of ~ 2.13 mM $CaCO_3$(s) at a pH of ~ 10.0 (Table S1-S3). Upon CO_3^{2-} consumption in Equation (3), HCO_3^- will be dissociated to restore the equilibrium in Equation (2), accompanied by the consumption of OH^-

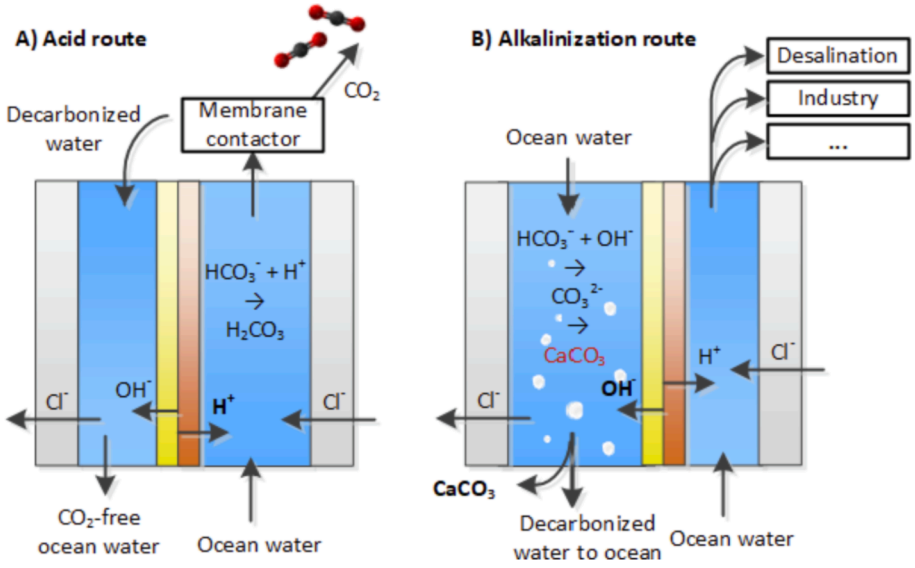

Fig. 1. Concept of CO_2 capture from the ocean water via electrochemical pH swing. A) CO_2 release using an acid route. B) CO_2 mineralization using alkalinization route.

ions, that in turn, decreases the solution pH.

The kinetics of above set of reactions are affected by the pH, temperature, and pressure [19]. In a well-mixed system with low mass transport resistances (at 25 °C, 1 atm, and pH 6), the carbonate-mineral precipitation step (Equation (3)) is the rate limiting step (with a time scale of 10^3 s, which is > 10^5 times slower than Equation (1) and (2) [17,25]).

Calcium carbonate ($CaCO_3$) precipitates in three anhydrous polymorphs including, in the order of thermodynamic stability, calcite (rhombohedral) > aragonite (orthorhombic) > vaterite (hexagonal) [24,25], in addition to its hydrated form. The thermodynamically favorable state is indicated by the saturation index (see EquationS1); a positive saturation index allows precipitation [26,27]. Fig. 2 maps the saturation index for the pH of typical seawater composition. To selectively precipitate carbonate minerals but avoid hydroxides precipitation (especially brucite $Mg(OH)_2$ that can precipitate with a much faster rate than $CaCO_3$), a base-pH < 10 should be maintained. On the other hand, within the pH range of 9.3 – 10, since the saturation index of $CaCO_3$ polymorphs still increases slightly with pH (Fig. 2, black curves), the higher limit (i.e., pH 9.6–10) is more desired, and is therefore chosen in this work as the optimum alkaline-pH window. See the supporting information for more details on the precipitation prediction.

3. BPM-induced pH-swing

The alkaline pH is the key parameter for facilitating the oceanic CO_2 capture through carbonate mineralization; a high pH increases the concentration of CO_3^{2-} ion (among other DIC forms), the $CaCO_3$ saturation index and kinetics of Equation 1–3. Using a bipolar membrane, the total concentration of the produced OH^- ions in the base compartment (determining pH_{Base}), assuming a coulombic efficiency of 100 % and ideally selective membranes can be calculated via [31]:

$$\left[OH^-_{produced}\right] = \left[H^+_{produced}\right] = \frac{(i - i_{lim})}{F}\left(\frac{t_r}{d}\right) \quad (4)$$

where $[OH^-]$ is the hydroxide ion concentration (mol m^{-3}), t_r the cell residence time (s), d the cell compartment thickness (m), i the applied electrical current density (A m^{-2}), i_{lim} the BPM-limiting current density (A m^{-2}), and F the Faraday constant 96485 (C mol^{-1}). The term $\frac{t_r}{d}$ is interchangeable with $\frac{A_m}{q}$, with A_m the membrane active area (m^2) and q the flow rate (m^3 s^{-1}) [31].

For current densities lower than the limiting current density i_{lim}, the water dissociation reaction (WDR) in the bipolar membrane is not dominant yet, decreasing the coulombic efficiency of the process due to the salt ion crossover through the BPM [8,32]. In other words, due to the non-ideal selectivity of the BPM and slow WDR kinetics at the low current density regime, the ion crossover dominates the water dissociation at low current densities [32]. For simplicity, we assume that the first ($\sim i_{lim}$) part of the applied current ($<i_{lim}$) is not contributing to a pH-swing. By manufacturing BPM's with high selectivity (to decrease the salt ions crossover), and high WDR-catalysts activity (i.e., fast WDR kinetics) one can reduce the limiting current density [33].

To remove carbonate ions efficiently, the produced OH^- ions (Equation (4)) must only be used to convert the bicarbonate ions in the seawater feed stream to CO_3^{2-} ions rather than forming hydroxide precipitates. Therefore, the process parameters e.g., the current density and cell residence time must be carefully tuned in such a way that the precipitation of hydroxide minerals, e.g., $Ca(OH)_2$ and $Mg(OH)_2$, are avoided.

4. Experimental section

4.1. Reagents and materials

Synthetic seawater was made with ionic compositions shown in Table 1. For simplicity, minor present ions such as strontium (Sr^{2+}) and bromide (Br^-) were excluded from the synthetic seawater mix, while the difference in the total salinity was made up for by adding NaCl salt instead. All reagents were of analytical grade acquired from VWR or Sigma Aldrich. During the experiments, all solutions were kept at ambient temperature of 23 °C ± 2 °C.

To avoid pre-precipitation (of e.g., $CaCO_3$), two separate feed tanks were used with their content mixed using T-connections right before

Table 1
Ion composition of the synthetic seawater as used in simulations and experiments. See the supporting information for the underlying calculations (Table S5, S6). The simulated feed pH is 8.104 (for a closed system).

Ion	mol/L	Ion	mol/L
Chloride (Cl^-)	0.5363	Calcium (Ca^{2+})	0.0102
Sodium (Na^+)	0.4593	Magnesium (Mg^{2+})	0.0521
Sulphate (SO_4^{2-})	0.0275	DIC	0.00215
Potassium (K^+)	0.0097	Proton (H^+)	0.002

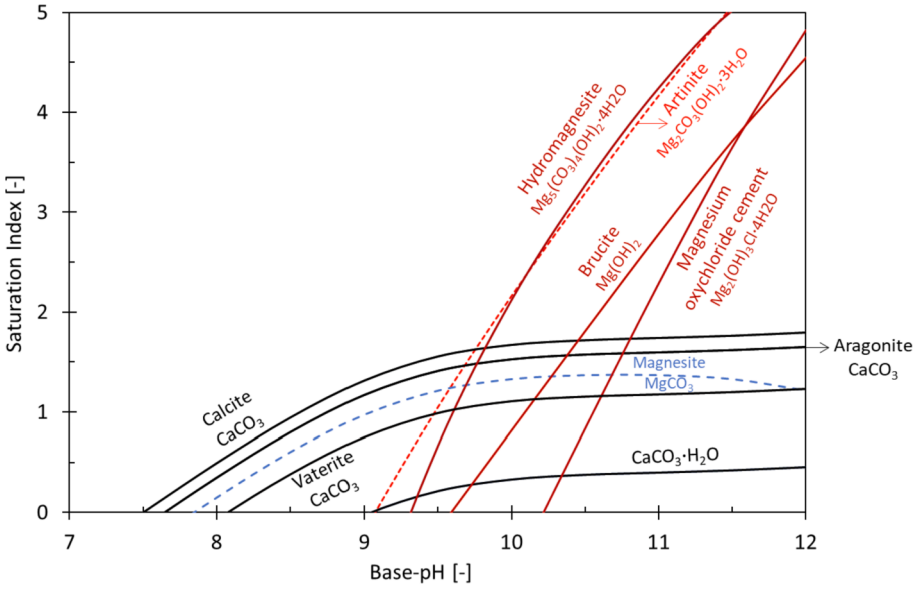

Fig. 2. The saturation index (SI) of all thermodynamically possible minerals in synthetic seawater vs. the base-pH, determined by Visual MINTEQ at 25 °C, based on the synthetic seawater compositions (Table 1) and assuming a closed system with no precipitation allowed during the pH-sweep. Minerals containing hydroxide ion (red), calcium carbonate (black), and magnesium carbonate (blue) are shown. Dolomite $CaMg(CO_3)_2$ [28] and Huntite $Mg_3Ca(CO_3)_4$ [29] are excluded from the graph due to their extremely slow kinetics at ambient temperature and pressure (in absence of any microbial activities). Calcium hydroxide $Ca(OH)_2$ does not occur as it stays undersaturated in the demonstrated pH range < 12 [30].

entering the electrochemical cell, and not any sooner. Feed tank 1 contain ~ 47 g L^{-1} NaCl, 0.385 g L^{-1} $NaHCO_3$, 1.45 g L^{-1} KCl, and 7.8 g L^{-1} Na_2SO_4 salt while feed tank 2 contain 3 g L^{-1} $CaCl_2.2H_2O$ plus 21.2 g L^{-1} $MgCl_2.6H_2O$. When each feed tank reaches equilibrium with the atmospheric CO_2 (420 ppm) and upon mixing the two feed streams, the corresponding synthetic seawater ion concentrations, which is also the starting point for all simulations, will become as shown in Table 1 (see Visual MINTEQ calculations procedure in Table S5, S6). Note that, upon equilibration with the atmospheric CO_2, part of the initially added DIC (in the form of sodium bicarbonate salt) leaves the solution as CO_2(g), increasing the feed pH and lowering the remaining net DIC-concentration to ~ 2.15 mM (instead of initially added 2.3 mM). Since adding more $NaHCO_3$ in tank 1 (to make up for the lost DIC to the air) would come with the cost of a higher $CaCO_3$ pre-precipitation when tank 1 and tank 2 are mixed, it is avoided in our work.

Similar to the synthetic seawater, the real seawater is supersaturated with respect to calcite and aragonite even before entering the BPMED cell, with thermodynamic calculations predicting a subsequent aragonite precipitation [34]. However, in real seawater, as opposed to the synthetic seawater, due to the presence of soluble organic matter interacting onto surface of crystals such inorganic precipitation is limited and almost absent [35,36].

In this work, in addition to the synthetic seawater, experiments using real seawater from the Wadden Sea, pre-treated with a 10 μm filter, was also conducted. In comparison with the synthetic seawater, the real seawater had a lower conductivity (35 mS cm^{-1} vs. 50 mS cm^{-1}), but a higher initial DIC-concentration (2.7 mM vs. 2.1 mM), see Table S7 for full ion composition.

4.1.1. Experimental setup

Two different electrochemical cells were used: (A) a six-compartment cell with a (single) BPM and (B) an upscaled BPMED cell containing 10 BPM-CEM cell pairs provided by REDstack B.V. (Table 2 and Fig. 3).

All solutions were pumped through the stack by peristaltic pumps (Cole-Parmer, Masterflex L/S Digital drive, USA), through 6.0 mm PTFE tubing (EmTechnik). The pH of the feed and outflow streams of the BPMED cell were measured every 2 s, using Orbisit CPS11D-7BA21 pH probes connected to a Liquiline CM444 digital multiparameter transmitter, both from Endress + Hauser, with an accuracy of ± 0.2 pH-units. All membranes used in the BPMED cells were provided by FuMATech B. V. The FBM-130, FKB-PK-130 and FAB-PK-130 were used as bipolar membranes (BPM), cation exchange membranes (CEM) and anion exchange membranes (AEM), respectively. Electrodes of titanium mesh coated with platinum, provided by MAGNETO Special Anodes B.V. (Schiedam, The Netherlands) were used in both cells.

4.1.2. Experimental procedure

The experiments were conducted under ambient temperature and pressure, in a one-way single pass continuous mode. To determine the required optimum alkaline-pH, five constant current densities of 10, 20, 30, 40 and 50 mA cm^{-2} were applied for 15 min to the thick six-compartment cell with a (single) BPM (Fig. 3 A). A constant flow rate of 120 ml min^{-1} (i.e., t_r = 11 s) was applied for those cases. After observing the *in situ* mineralization in the short experiments, longer experiments of 120 min were conducted at i = 10 and 40 mA cm^{-2} to determine membrane fouling and energy consumption of the process. For those samples, the BPM was prepared (see Membrane fouling and crystal analysis) for the Scanning Electron Microscopy (SEM) coupled with energy dispersive X-ray spectroscopy (EDS) (JEOL-6480LV, JEOL Ltd., Japan) analysis.

In the thin upscaled BPM-CEM stack (Fig. 3 B), constant current density of 5 mA cm^{-2} and a liquid flow rate of 68 ml min^{-1} per compartment (i.e., t_r = 3.53 s) were applied for 30 min. This combination of the current density and flow rate in the upscaled stack was chosen based on the earlier results obtained from the six-compartment cell with a (single) BPM.

After each experiment, the stack was rinsed thoroughly with 1 mM HCl solution followed by demineralized water to remove any fouling. Each experiment was performed at least three times.

Table 2
Summary of the properties of electrochemical cells used in this work.

Electrochemical stack	A_m (cm^2)	Compartment volume (cm^3)	Aim
A) Six-comp. cell with a single BPM, 1 cm thick compartment, no spacers	22	11 × 2 × 1 = 22	*In situ* observation of the electrochemical mineralization due to thick compartments, plus BPM fouling studies
B) Thin upscaled cell, integrated gasket mesh spacers of 400 μm (Aqua Battery B.V.)	100	10 × 10 × 0.04 = 4	Upscaling and energy consumption measurement, incl. real seawater tests

4.1.3. Precipitation collection incl. Seeding

Seed addition enhances the kinetics of carbonate crystallization [27,37]. In the six-compartment cell with a (single) BPM, when the pH in the acid compartment was stable, ca. 200 ml sample was taken directly from the output of the base compartment. This content was divided over three bottles (50 ml each): where in one, 0.5 g solid calcite seeds (AquaMinerals B.V., particle size of 0.2 – 0.4 μm) where added (resulting in 10 g L^{-1}), one where 0.5 g solid lime pellets (AquaMinerals B.V., particle size ≤ 3 mm) where added (i.e., to get 10 g L^{-1}) and the last one with no seeding. The bottles were closed to avoid contact with the atmospheric CO_2 and left undisturbed for at least 72 h. In the upscaled cell, the total produced base-volume was gathered in storage tank, left undisturbed for ≥ 72 h.

4.1.4. Membrane fouling and crystal analysis

In the six-compartment cell with a (single) BPM, after applying current densities of 10 and 40 mA cm^{-2}, the AEL surface of the BPM was analyzed by the Scanning Electron Microscopy (SEM) coupled with energy dispersive X-ray spectroscopy (EDS) (JEOL-6480LV, JEOL Ltd., Japan) to determine the fouling of the membrane. After disassembling the cell, the BPM was washed with demineralized water and left at ambient temperature to be dried before SEM/EDS analysis. The samples were coated with gold using a JEOL JFC-1200 Fine coater at 10 Pa for 30 s.

The solid precipitate within the "alkaline gathering tanks" (obtained after carefully decanting the liquid and air-dried) were scraped on a microscope slide glass for Raman spectroscopy analysis. Raman spectroscopy (Horiba Jobin-Yvon LabRAM HR) was done using 532.13 nm laser within 10–100 s time spots.

4.2. Data analysis

4.2.1. DIC, Ca^{2+} and Mg^{2+} removal rates

The DIC concentration of the feed and alkaline streams were determined via titration with 0.1 M HCl (see Figure S1 and Table S8). However, this method is sensitive to atmospheric CO_2, meaning that the DIC concentration can be slightly over- or underestimated depending on the sample pH. Therefore, in addition to the DIC removal, Ca^{2+} and Mg^{2+} ions removal was also measured, using Inductively Coupled Plasma (ICP). For both analyses, the liquid samples were first filtered through a MF-Millipore™ Filter with a pore size of 0.22 μm to remove any formed minerals.

4.2.2. Energy consumption

The total electrical energy consumption E (kJ mol^{-1} DIC) required for the *in situ* mineralization is:

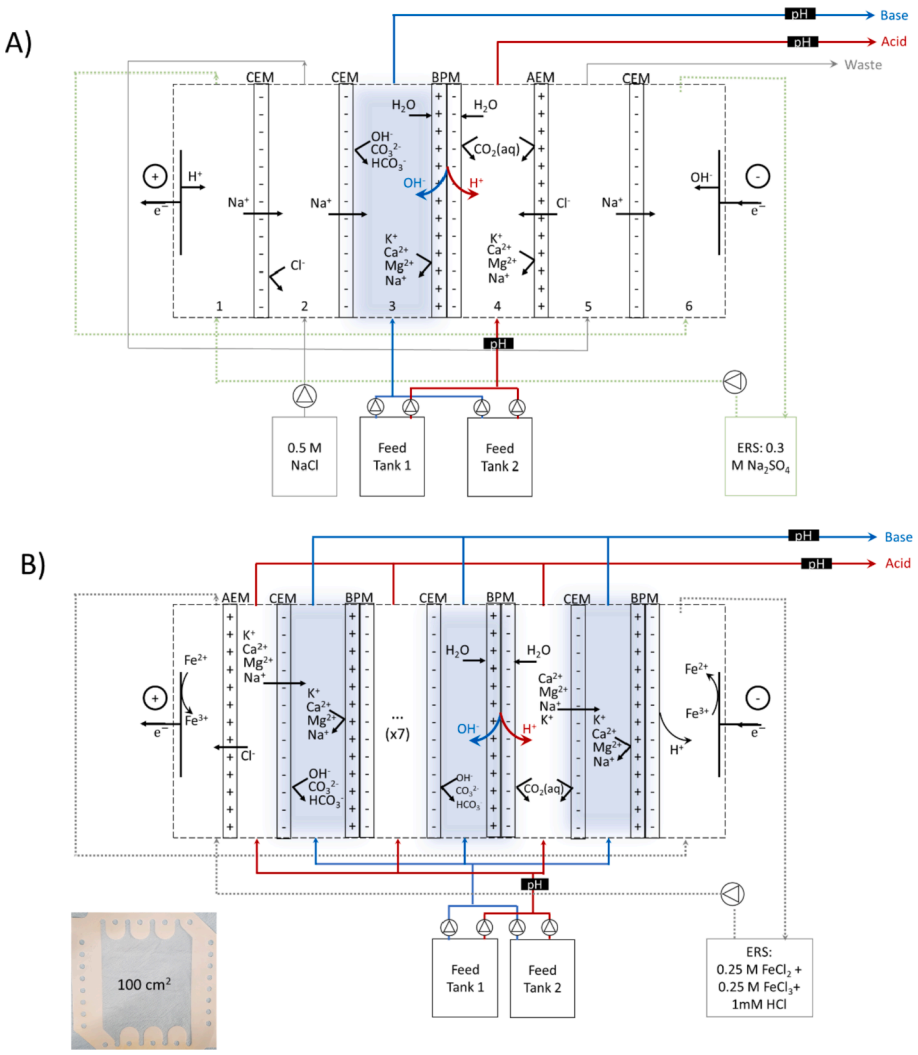

Fig. 3. Graphical representation of the (A) six-compartment BPM cell demonstrating the compartment numbers, and (B) the BPM-CEM stacked upscaled cell (with 10 cell pairs) with the integrated 400 μm gasket-mesh spacer and blue cell-unit shown. Feed tank 2 contains $CaCl_2$ and $MgCl_2$ and Feed tank 1 contains remaining salts from Table 1. ERS is the electrode rinsing solution. For the tests with the real seawater, tanks 1 and 2 were replaced with a single seawater feed tank accompanied with 10 μm filter. In (B), a shielding AEM is used next to the anode, to avoid $Fe(OH)_2$ precipitation.

$$E = \frac{\int_{t_0}^{t_{end}} UIdt}{m_{DIC}} \approx \frac{UI\Delta t}{q\Delta t R_{DIC}[DIC_i]} \quad (5)$$

where I is the applied current density (A), U the total cell voltage (V), and $\Delta t = t_{end} - t_0$ the experiment duration (s). m_{DIC} is the extracted carbonate mineral (mol) that is calculated using q the total liquid flow rate considering all base compartments (L s^{-1}), $[DIC_i]$ the initial dissolved inorganic carbon concentration in the feed (mol L^{-1}), and R_{DIC}

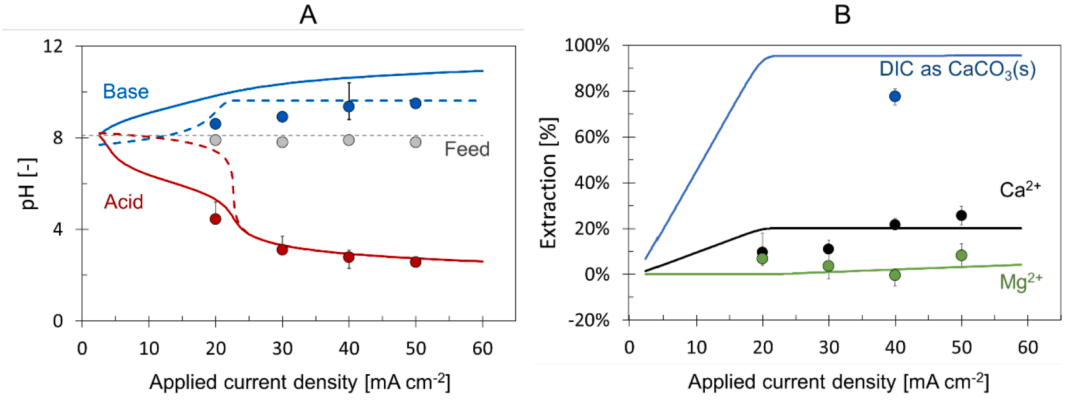

Fig. 4. Comparison of the simulated (lines) and experimentally obtained values (bullets) at each applied current density in the six-compartment cell with a (single) BPM, averaged over the experiment duration and (four) repetitions (for simulation data see Table S9). In (A) Dashed lines show the (simulated) pH-change after DIC-extraction as CO_2(g) (red) and $CaCO_3$(s) (blue). Error bars show the margin between the minimum and maximum experimental data points to include all data. The error bars that are not shown are smaller than the data points. The cell residence time is $t_r = 11$ s for all cases (i.e., flow rate q = 120 ml min^{-1}, flow velocity $v = 1$ cm s^{-1}), and $i_{lim} = 2.5$ mA cm^{-2} is assumed. (A) outflow-pH and feed-pH from the cell vs. the applied current density, (B) species removal at each applied current density where the single measured DIC-removal point is shown (blue bullet) as an indication.

the DIC removal (%) measured via acid titration with $R_{DIC}[\%] = \frac{[DIC_i]-[DIC_e]}{[DIC_i]}$), and $[DIC_e]$ (mol L^{-1}) the remaining end DIC concentration after precipitation (>72 h). The simplification of the integration in left-hand side of Equation (5) is possible when a constant voltage, current, flow rate and R_{DIC} is assumed throughout the whole duration of the experiment.

5. Results and discussion

5.1. Effect of the current density and pH

To validate the pH range that is most effective for carbonate precipitate removal, we demonstrate the effect of applied current density, while keeping the residence time (t_r) constant, using the six-compartment cell with a single BPM. Fig. 4 compares the experimental and simulated values. The simulation assumptions and procedures are shown in the supporting information (Table S9).

The experimentally obtained acid-pH agrees well with the simulated-pH line without CO_2(g) extraction (Fig. 4A-red circles and red lines), supporting our assumption of a high columbic efficiency of the bipolar membrane at the tested current densities; when using Equation (4), if the columbic efficiency is low, the amount of the produced acid will be less than expected, which is not the case here. Similarly, the experimental feed-pH is constant at pH 7.9 and in close agreement with simulations which was pH 7.7–8.1 (Fig. 4A-grey line). The acid data point at 20 mA cm^{-2} also demonstrates that the experiments are better predicted by the solid line (representing no *in situ* CO_2(g) extraction) than by the dashed curve (simulation where CO_2(g) is extracted during the BPMED process) in Fig. 4A. This corresponds to our approach in this work, where no attempt for gaseous CO_2(g) extraction is taken (and no spontaneous CO_2 gas bubbles are extracted *in situ*).

The experimental base-pH are 1.2–1.4 pH-units lower than that simulated without considering any DIC-extraction (Fig. 4A-blue bullets vs. lines). However, for the base compartment, the simulation when including *in situ* precipitation (dotted blue lines in Fig. 4A) is close to the experimental value. This can also be expected from theory: while the acid compartment does not exceed the solubility of CO_2 in seawater surface (33 mM at 3.5 % salinity, 1 atm and 20 °C) [38], the solubility of carbonate CO_3^{2-} is far exceeded (i.e., > 47x of 2.15 mM) in the base stream, which causes *in situ* mineral formation. The carbonate solubility in seawater is ca. 0.0451 mM, calculated assuming seawater-K_{sp}^{CaCO3} = 4.39×10^{-7} (mol per kg SW)^2 at salinity of 3.5 % at 1 atm, 25 °C [39], and Ca^{2+} concentration based on Table 1.

Even after correcting for the effect of precipitation on the base-pH, a small difference of ≤ 0.5 pH-unit exists between the measured and calculated values at current densities ≤ 30 mA cm^{-2}. The origin of this remaining 0.5 pH-unit difference can be because of the local spots of high carbonate or OH^- concentrations within the cell. Although in the simulations a uniform pH and ions distribution are assumed, the OH^- ion concentration is higher next to the BPM surface than the bulk. As a result of this locally high concentration spots, if the produced OH^- ions partly precipitate at $Mg(OH)_2$, the end-pH lowers. Subsequently, such precipitation increases the resulted Mg^{2+} ions removal while decreasing the Ca^{2+} removal compared to the simulations. This is also confirmed from the ion removal analysis (Fig. 4B), which shows more Mg^{2+} and less Ca^{2+} removal (in the experiments) compared to simulations at i ≤ 30 mA cm^{-2}. Improving the mixing inside of the cell, using e.g., mesh spacers enhance the uniformity of ionic distributions.

Theoretically, for i ≥ 20 mA cm^{-2}, ≥ 94 % of the DIC can be extracted as $CaCO_3$ (Fig. 4B and Table S9). Similarly, if we calculate the DIC extraction from the experimentally measured Ca^{2+} ion removal at i = 40 mA cm^{-2} (i.e., removal of 2.079 mM Ca^{2+} ion), assuming all Ca^{2+} is removed as $CaCO_3$(s), ca. 97 % of the DIC is extracted. However, at i = 40 mA cm^{-2}, the extracted DIC is measured to be between 74 and 81 % through HCl titration (Fig. 4B-blue circle). Such deviation is partly due to the inaccuracy of the titration method to determine the DIC concentration (hence, we deem estimation via Ca^{2+} and Mg^{2+} removal by ICP more accurate than direct DIC removal measurement through HCl titration), and partly due to the side-precipitations taking place due to a non-uniform ionic distribution, as explained above.

5.2. Towards industrial scales: Decreasing the energy consumption

To decrease the process electrical energy consumption, the total cell voltage must be reduced while the $CaCO_3$ production is unchanged/improved. Furthermore, for mineralization, the optimum base-pH must be facilitated by accurate controlling the applied current density and flow rate (Equation (4)). Prior to the upscaling, the theoretical relation between $CaCO_3$ production rate (i.e., extracted $CaCO_3$ in kg h^{-1} m^{-2} which is normalized for the membrane area) and applied current density was studied for the BPM-CEM cell to find the optimum combination that provide the lowest electrical energy consumption (Fig. 5). The calculation model is given in the supporting information (see Equation S4-S7). For estimating the thermodynamic energy required in BPMED based capture, the voltage of the bipolar membrane (V_{BPM}) is calculated via Nernstian voltage of 0.059ΔpH [40].

Fig. 5B shows that at a fixed base pH 10.0, the $CaCO_3$ production increases with the current density. Given the limited DIC, a maximum of ca. 2.078 mM $CaCO_3$ (= 208 mg per L) is extractable from seawater. Therefore, the increase in the production is merely the result of a higher flow rate (i.e., lower cell residence time) at higher current densities; to maintain a constant base-pH (in this case, pH 10.0), a linear relation between the current density and flow rate exists (Equation (4)). However, the electrical energy consumption also increases upon increasing the current density due to ohmic losses of ΔV = IR (Fig. 5A-blue line).

The thermodynamic electrical energy consumption for $CaCO_3$ production is 35 kJ mol^{-1} $CaCO_3$ (i.e., 0.097 kWh kg^{-1} $CaCO_3$, Equation S4), Fig. 5A. Since an *in situ* process enables CO_2 capture and recovery in a mild pH-swing, it can perform theoretically at the Nernstian voltage of V_{BPM} = 0.059 × (10.0 – 4.5) ~ 0.3245 V, while 0.83 V is thermodynamically required for extreme ΔpH = 14 in *ex situ* cases, decreasing the required energy for the pH-swing by a factor of almost three. Although the membrane voltage is in reality higher than its theoretical voltage for mild pH gradients, the reversible BPM voltages are still < 0.83 V for an *in situ* process, even at 25 mA cm^{-2} [31]. Moreover, as opposed to the *ex situ* process, in an *in situ* capture, no highly concentrated chemicals (i.e., NaCl, NaOH) are needed in the process.

Unfortunately, currently available BPM's are not developed to take full advantage of a mild-pH environment yet and, therefore, dissociate water at V_{BPM} ≥ 0.6 V in practice for current densities > 5 mA cm^{-2}. In addition, the charged membranes and electrolyte compartments suffer from significant ohmic losses, which increase with the current density (i.e., ΔV = IR). The practical energy consumption of the carbonate mineralization via *in situ* pH-swing, including these voltage losses, is >5x higher than the thermodynamic value. Aiming for the lowest energy consumption, ohmic losses should be limited, marking the optimum current density for the BPM-CEM cell somewhere between i = 5-10 mA cm^{-2} in our system (Fig. 5A).

For reducing the process energy consumption, the cell design and membrane configuration are also crucial. Fig. 6 shows the voltage and energy required for each component within the electrochemical cell, obtained from our experiments. To allow comparison between the cases, the measured base-pH is kept identical (9.6–9.8) for all four cases. The energy consumption normalized to the produced moles of $CaCO_3$ is shown in Fig. 6B.

Ideally, all electricity input is used to dissociate water into H^+ and OH^- production at the BPM (creating the ΔpH over the BPM) at a thermodynamic reversible potential (i.e., 0.059ΔpH), while the irreversible losses are nullified. This implies that the dark red segment (showing the thermodynamic BPM-voltage) in Fig. 6 should be the only/highest portion of the cell voltage. Although the 10-cell BPMED stacks

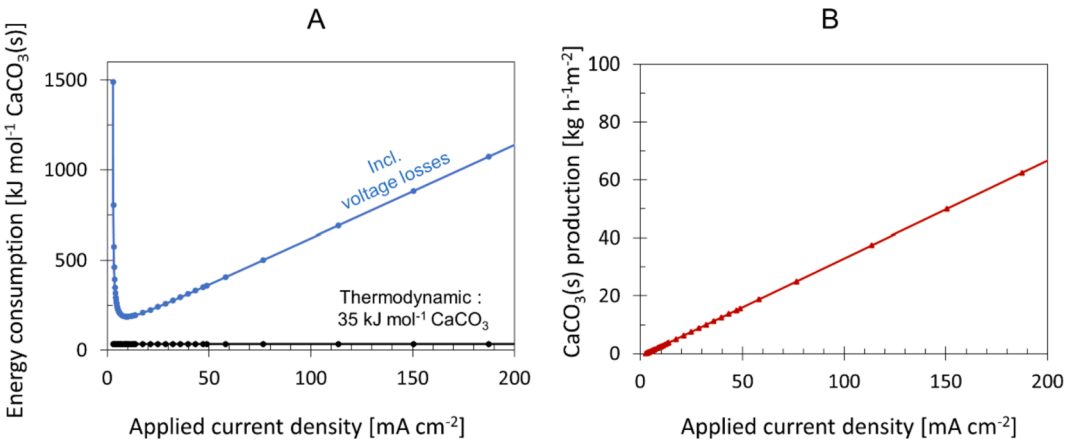

Fig. 5. Relation between the applied current density vs. (A) electrical energy consumption and (B) calcium carbonate normalized production rate. Simulations are done assuming a 10 × 10 cm^2 BPM-CEM cell containing 10 cell pairs and base-pH 10.0 (i.e., produced OH^- ions of 0.0023 M, see Table S1). The value of the thermodynamic limit is obtained using the Nernstian membrane voltage for required ΔpH = 5.5; see Equation S4.

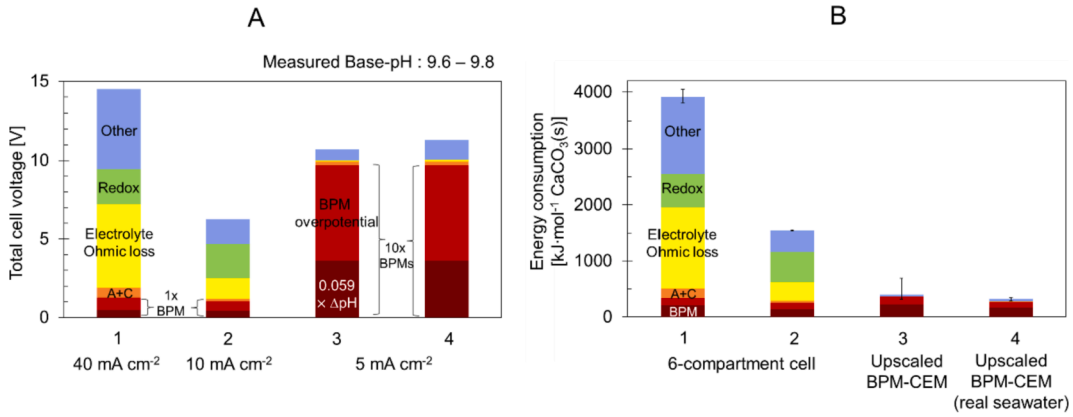

Fig. 6. A) Total cell voltage and its components, from bottom to top: BPM thermodynamic voltage (0.059ΔpH, dark red), BPM-overpotential (red), monopolar membrane (AEM and CEM) ohmic loss (orange: A + C), electrolyte ohmic loss (yellow), the redox reactions (green), and other losses (blue) in the six-compartment cell with a single BPM. Case 1 and 2 both incl. 1 BPM while the upscaled BPM-CEM cell (case 3, 4) both include 10 BPM's. B) The energy consumption and its components (from bottom to top same as A). In all the cases, the amount of charge added per volume via the BPM is ~ 220–413 C L^{-1}. Case 4 is tested via real seawater (Table S7), while other cases are done using synthetic seawater (Table 1). Error bars in B mark the minimum and maximum values among repetitions.

are more effectively using the cell voltage for water dissociation (i.e., relatively large dark red segment), irreversible losses still occur. Most notably, the BPM overpotential (light red contribution) exceeds the thermodynamic BPM voltage. This BPM overpotential is the difference between the measured BPM-voltage and the thermodynamic-BPM voltage and reveals the overpotential including ohmic losses and WDR overpotential of the BPM. "Other" involved losses (blue) are defined here as the difference between the measured and theoretically expected cell voltage. These losses include e.g., H_2/O_2 gas bubbles /covering the electrodes (for case 1, 2), possible CO_2(g) bubbles/ trapping in the acidic compartment of the BPMED [25], membrane/spacer fouling, and mesh spacers reducing the active membranes area (for case 3, 4).

In the six-compartment cell with a (single) BPM, reducing the current density from 40 to 10 mA cm^{-2} (case 1 to 2, charge added per volume 413 to 330 C L^{-1}), already decreases the cell voltage contributions of the electrolyte compartments and the "other" portion. However, to keep the base-pH identical, a four times lower flow rate was used in case 2 compared to case 1. While a lower flow rate increases the cell residence time (t_r), allowing more time for *in situ* precipitation, it is less effective in "cleaning away" the formed minerals within the cell compartments, increasing the risks of fouling. Furthermore, the $CaCO_3$ production rate is lower when using a lower flow rate (Fig. 7C, case 2). Case 3 and 4 (Fig. 6B) achieve a lower energy consumption by decreasing the compartment thickness (25x), increasing the number of cells, changing the redox couple from water to $FeCl_2$/ $FeCl_3$, and eliminating the AEM from the cell design with only BPM-CEM cell pairs remaining.

The achieved energy consumption of 318 ± 29 kJ mol^{-1} $CaCO_3$ (i.e., ca. 0.88 kWh kg^{-1} $CaCO_3$) for the real seawater case in this work is the lowest achieved using an electrochemical cell for carbonate removal, ever [6]; in other works, the lowest electrical energy required for (*ex situ*) BPM-based oceanic calcium carbonate removal is calculated to be ≥ 640 KJ mol^{-1} $CaCO_3$(s) [4,10], with experimental reported values of 1080–2880 KJ mol^{-1} $CaCO_3$(s) [16] and 1009–2162 KJ mol^{-1} $CaCO_3$(s) [41]. In a broader context, the energy consumption range for electrochemical captures is demonstrated at 56–6940 kJ_e mol^{-1} CO_2 [6]. This is while, assuming an average worldwide carbon emission for electricity of ca. 0.46 kg CO_2-eq kWh_e^{-1} (=0.0029 mol CO_2-eq kJ_e^{-1}), the required energy for capturing must not exceed 344 kJ_e mol^{-1} CO_2 or electricity from renewable sources (i.e., zero electricity-emission sources) must be used.

However, the electric energy consumption of electrochemical CO_2 capture is still high, especially compared to the fossil fuel combustion energy which is 300–700 KJ mol^{-1} of emmitted-CO_2(g) [8]. Considering the thermodynamic electrical energy consumption (35 kJ mol^{-1} $CaCO_3$), there is room left for improvements. In BPMED-capture, approximately 90 % of the electrical energy is used in the BPM

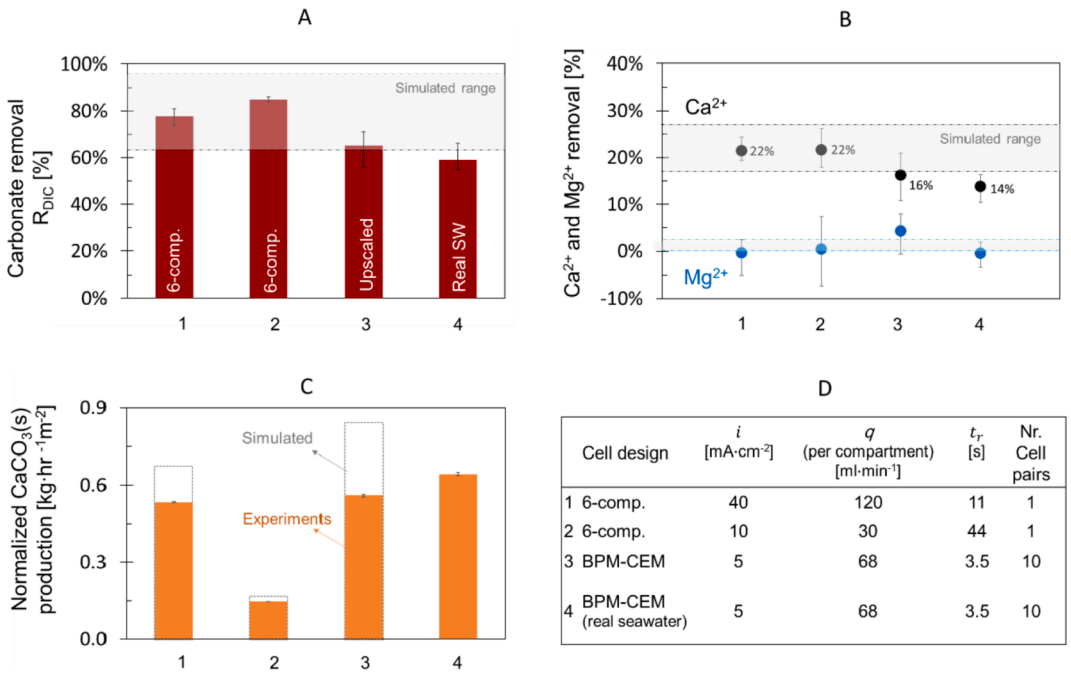

	Cell design	i [mA·cm^{-2}]	q (per compartment) [ml·min^{-1}]	t_r [s]	Nr. Cell pairs
1	6-comp.	40	120	11	1
2	6-comp.	10	30	44	1
3	BPM-CEM	5	68	3.5	10
4	BPM-CEM (real seawater)	5	68	3.5	10

Fig. 7. Comparison of the six-compartment cell with a (single) BPM (case 1 and 2) and upscaled BPM-CEM cell (case 3 and 4) performance with regards to (A) carbonate (i.e., DIC) removal, (B) Ca^{2+} and Mg^{2+} ions removal, and (C) normalized calcium carbonate production. Process properties are shown in D, in which q is the flow rate in each compartment. Error bars show the margin between the minimum and maximum data points. For simplicity, all simulations are based on the synthetic seawater compositions (Table 1) and not the real seawater (i.e., case 4). The simulation data is shown in Table S10-S11. The simulations are not done for the real seawater case due to the complexity of that system.

(Fig. 6-case 3, assuming a WDR-voltage of 0.9 V and BPM-area resistivity of 8 Ω cm^2). Decreasing the WDR-voltage to its thermodynamic value of 0.059ΔpH, decreases the energy consumption by a factor of 3. Utilizing a properly catalyzed BPM (i.e., fast WDR kinetics), with highly perm-selective ion-exchange layers to exclude co-ions, and with optimum thickness of the layers and the catalyst is therefore most effective way to minimize energy losses [32]. Furthermore, increasing the DIC-removal (from measured 65 % to 95 %) can decrease the total energy consumption by 59 %, but might come at the expense of lower coulombic efficiency for $CaCO_3$ production.

The extraction rate of the dissolved inorganic carbon (DIC), calcium (Ca^{2+}), and magnesium (Mg^{2+}) ions, and the normalized calcium carbonate production for the four tested cases are shown in Fig. 7. In all cases, the product of the seawater alkalinization with base- pH between pH 9.6 – 10 is mainly aragonite ($CaCO_3$), as expected [42] and confirmed with Raman spectroscopy (Figure S2). The simulations data for case 1–4 are shown in Table S10-S11.

The measured carbonate removal (R_{DIC}) for all cases is within the expected range of 63 – 97 % (grey box in Fig. 7A), confirming our model and its underlying assumptions. The lower margin of 63 % corresponds to simulations assuming an open system, where the alkaline solutions keep absorbing CO_2(g) from the atmosphere until it reaches equilibrium. The 97 % margin is for a fully closed system. In an open system, the end-pH after precipitation and the total DIC-extraction are lower compared to a closed system. In the experiments, the electrochemical cell and crystallization tanks are kept closed to avoid the contact with the atmospheric CO_2(g). However, such contact during sampling and titration (to determine DIC-concentration) cannot be avoided, making the system somewhere between fully closed and fully open.

In general, it was expected that adding calcite/ lime seeds in the gathering tanks increase the carbonate removal slightly, but although the seed may have sped up the precipitation process, the chosen settling time (≥72 h) was apparently long enough to reach equilibrium in all cases in this work. The upper margins of the error-bars in Fig. 7A show the R_{DIC} values obtained using seeding, which is slightly higher compared to without seeding. In Fig. 7A, case 2 has the highest carbonate removal, with values slightly higher than case 1, but the Ca^{2+} and Mg^{2+} removal for both cases are identical (Fig. 7B, 1 and 2). Therefore, as both cases produced mainly Aragonite (confirmed with Raman spectroscopy), the slight difference in R_{DIC} between case 1 and 2 is probably resulted from imprecision of the titration method to quantify carbonate removal.

For the real seawater (case 4), R_{DIC} is the lowest, probably due to the difference in ion composition and concentration between real and synthetic seawater (i.e., initial DIC-concentration in seawater was 0.6 mM higher than that of the synthetic seawater). Moreover, in the real seawater, presence of elements such as Boron, Silicon, Sulphur, Nitrate (Table S7), and anti-scaling effects of organic substances can also influence the co-precipitation. This also justifies why Ca^{2+} removal is the lowest for case 4 in Fig. 7B.

The Ca^{2+} removal for case 3 (i.e., BPM-CEM cell) is ca. 16 %, which is lower than case 1 and 2 (Fig. 7B), but all values are still close to the simulated 20 % (for closed systems) and in the range of 17 – 27 % (for open systems) as shown in Table S10-S11. Furthermore, it seems that the lower Ca^{2+} removal in case 3 is compensated with a higher removal of Mg^{2+} for this case (Fig. 7B-blue marks). This is while the simulated Mg^{2+} removal for case 1 to 3 shows a decreasing trend (from 2 % to 0 % since the simulated pH decreases). Since the observed discrepancy between the cases is not expected in the simulations, it must originate from the experimental condition including the different cell design and flow pattern inside of the compartments in case 3; the latter creating non-uniform flow and thus non-uniform local pH. As for the cell design, in the six-compartment cell with a (single) BPM, only Na^+ ions pass through the CEM into the base-compartment, carrying the charge (Fig. 3A-from comp.2 to 3). However, in the upscaled cell containing BPM-CEM cell pairs (case 3), considering the concentration and mobility ratio of all five present cations, only 83 % of the current is carried via Na^+ ions transfer, while the contribution of H^+, K^+, Mg^{2+}, and Ca^{2+} are 2.5 %, 2.5 %, 10 % and 2 %, respectively, based on the Nernst-Planck equation (Table S12). We hypothesize that this additional Mg^{2+} ions

present in the base compartment hinders $CaCO_3$ mineralization (i.e., decreasing both Ca^{2+} and DIC removal), promoting $Mg(OH)_2$ precipitation instead. Even though this additional Mg^{2+} concentration is only 0.2 mM in the bulk, it can still promote $Mg(OH)_2$ mineralization near the membrane surface due to the concentration polarization on the CEM surface. The influence of the magnesium ion is well documented and is known to reduce calcite growth rates [43–46].

Comparing Fig. 7 A and B, if we assume all Ca^{2+} ions are extracted as $CaCO_3$, a Ca^{2+}-removal of 20 % translates into 97 % DIC-extraction, which is higher than what was measured. This proves that part of Ca^{2+} is removed as other solids e.g., as hydroxides (e.g., at BPM local-pH $\geq$ 12 [30]), even though this was not seen in Raman spectroscopy analysis (Figure S2). Furthermore, the accuracy of the titration method can play a role in justifying this discrepancy.

Despite the slightly lower DIC (i.e., carbonate) and Ca^{2+} ion removal in case 3 and 4 compared to the six-compartment cell with a (single) BPM, the energy consumption per removed $CaCO_3$ is still lower for the upscaled cell (Fig. 6B). In case 1 and 2, the energy consumption is high due to the voltage losses (i.e., thick compartments + water redox) and the fact that only one base-compartment exists (with ratio of base-compartment to rest-compartments 1:6), decreasing the $CaCO_3$ production rate significantly (Fig. 7C). Between case 3 and 4, real seawater had a smaller conductivity compared to the synthetic seawater (i.e., 35 mS cm^{-1} vs. 50 mS cm^{-1}) but higher initial DIC (i.e., 2.7 mM vs. 2.3 mM). Therefore, due to this higher initial DIC, despite of the lower relative DIC-removal (Fig. 7A), the absolute $CaCO_3$ production is still the highest for the real seawater case (Fig. 7C), making it also the most energy efficient case (Fig. 6B).

5.3. Fouling

While our *in situ* mineralization process shows a clear benefit for the energy consumption compared to the *ex situ* bipolar membrane electrodialysis (BPMED) (318 $\pm$ 29 kJ mol^{-1} $CaCO_3$, which is less than half of the lowest value in literature), the feasibility of the *in situ* process is strongly affected by the cell design and fouling. The fouling at the membrane and spacers: (1) increases the pressure drop along the cell, increasing the pumping energy and causing non-uniform flow, and (2) increases the total cell voltage and hence the electrical energy consumption. Furthermore, the membrane lifetime and $CaCO_3$ harvesting rate are negatively affected by fouling. To determine the membrane fouling, SEM and EDS analysis have been done for the six-compartment cell with a (single) BPM by opening the cell (right) after finishing the 15 min constant current (40 mA cm^{-2}) experiments (Figure S3, S4) and after the 2 h experiment (Fig. 8).

After opening the cell right after the 15 min constant current, only few minerals were seen on the membrane (Figure S4), which is logical considering the time scale of 10^3 s required for establishing the $CaCO_3$ precipitation equilibrium [17,25]. We observed that the amount of deposition is increased with current and the time of experiment. After 120 min experiments, the surface of the BPM is decorated with a layer of minerals (Fig. 8), even though the fouling does not increase the total cell voltage. The SEM analysis emphasizes the importance of fouling removal strategies for *in situ* mineralization.

Furthermore, when a low current density, in combination with a low flow rate, is applied for the 120 min constant current experiments, although the output pH remained the same, there is a clear difference in the shape of the minerals (Fig. 8 D-F vs. A-C). At 10 mA cm^{-2}, the minerals have a more defined "broccoli" shape that is the defined shape of Aragonite which is in accordance with Raman spectroscopy findings, while at 40 mA cm^{-2} the membrane surface is covered with polydisperse, polymorph particles. However, the effect of the cell residence time (i.e., flow rate) in the *in situ* bipolar membrane electrodialysis cell needs to be studied in more detail to draw a solid conclusion on the precipitation kinetics and type of the scaling. In addition to adjusting the flow rate to wash out the fouling, fouling removal strategies such as, gas sparging and acid wash can be employed in future works.

6. Conclusion

Through *in situ* mineralization enabled using bipolar membranes, Aragonite (polymorph of $CaCO_3$) was extracted from (real and synthetic) seawater as an ocean carbon removal strategy. By controlling the current density and cell residence time, >60 % of the dissolved inorganic carbon (DIC) and $\geq$ 16 % of the Ca^{2+} ion is extracted, without the need for any additional chemicals. An energy consumption of 318 $\pm$ 29

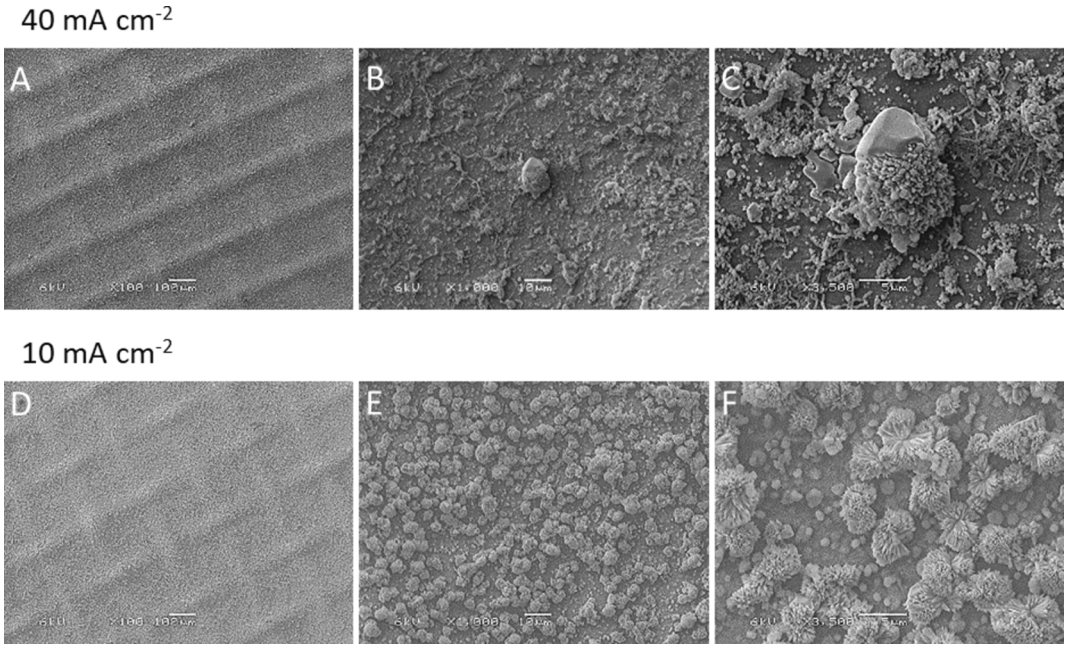

Fig. 8. SEM images of the AEL of the BPM opened directly after applying the current for 120 min. (A), (B) and (C) concern the AEL of the BPM after applying a current density of 40 mA cm^{-2} and a flowrate of 120 ml min^{-1} (v = 1 cm s^{-1}), resulting in a measured base-pH of ~ pH 9.8. (D), (E) and (F) concern the AEL of the BPM after applying a current density of 10 mA cm^{-2} and a flowrate of 30 ml min^{-1} (v = 0.25 cm s^{-1}), resulting also in a base-pH of 9.8.

kJ mol^{-1} $CaCO_3$ (i.e., ca. 0.88 kWh kg^{-1} $CaCO_3$) is obtained for DIC-capture from real seawater with $CaCO_3$ production rate of 0.64 kg $CaCO_3$ h^{-1} m^{-2}. Theoretically, at a mild-pH swing (e.g., base pH 10.0 and acid pH 4.5, thus $\Delta pH = 5.5$) the thermodynamic energy required to capture $CaCO_3$ though *in situ* mineralization is $\sim$ 35 kJ mol^{-1} $CaCO_3$ which is <10 % of that experimentally achieved. However, the irreversible BPM-overpotential is responsible for > 55 % of the required electrical energy. Focusing on membrane engineering to achieve fast WDR kinetics in the BPM, with highly permselective ion-exchange layers to exclude co-ions, and with optimum thickness of the layers is the most effective way to minimize energy losses. Despite the promising energy consumption, membrane fouling is a challenge that *in situ* mineralization process faces. In the future, fouling removal strategies such as gas sparging and acid wash can be employed for interval cell cleaning.

Declaration of Competing Interest

The authors declare that they have no known competing financial interests or personal relationships that could have appeared to influence the work reported in this paper.

Acknowledgements

This work was performed in the NWO-cooperation framework of Wetsus, Centre of Excellence for Sustainable Water Technology (www.wetsus.nl). Wetsus is funded by the Dutch Ministry of Economic Affairs, the European Union Regional Development Fund, the Province of Fryslân, the City of Leeuwarden and the EZ/Kompas program of the Samenwerkingsverband Noord-Nederland". The authors like to thank the participants of the research theme "Concentrates" in Wetsus and research groups "Transport phenomena" and "Electrochemical flow systems" in faculty of applied sciences at TU Delft for the discussions and their (financial) support. This research received funding from the Netherlands Organization for Scientific Research (NWO) in the framework of the project ALW.2016.004.

Appendix A. Supplementary data

Supplementary data to this article can be found online at https://doi.org/10.1016/j.cej.2022.135326.

References

[1] A.G. Fane, A grand challenge for membrane desalination: More water, less carbon, Desalination 426 (2018) 155–163.
[2] M. Eisaman *et al.*, "Energy-efficient electrochemical CO2 capture from the atmosphere," *Tech. Proc. 2009 Clean Technol. Conf. Trade Show*, pp. 5–8, 2009.
[3] F. Sabatino, et al., Evaluation of a Direct Air Capture Process Combining Wet Scrubbing and Bipolar Membrane Electrodialysis, Ind. Eng. Chem. Res. 59 (15) (Apr. 2020) 7007–7020.
[4] C.-F. de Lannoy, M.D. Eisaman, A. Jose, S.D. Karnitz, R.W. DeVaul, K. Hannun, J.L. B. Rivest, Indirect ocean capture of atmospheric CO2: Part I. Prototype of a negative emissions technology, Int. J. Greenh. Gas Control 70 (2018) 243–253.
[5] I.A. Digdaya, I. Sullivan, M. Lin, L. Han, W.-H. Cheng, H.A. Atwater, C. Xiang, A direct coupled electrochemical system for capture and conversion of CO2 from oceanwater, Nat. Commun. 11 (1) (2020), https://doi.org/10.1038/s41467-020-18232-y.
[6] R. Sharifian, R.M. Wagterveld, I.A. Digdaya, C. Xiang, D.A. Vermaas, Electrochemical carbon dioxide capture to close the carbon cycle, Energy Environ. Sci. 14 (2) (2021) 781–814.
[7] J.H. Rheinhardt, P. Singh, P. Tarakeshwar, D.A. Buttry, Electrochemical capture and release of carbon dioxide, ACS Energy Lett. 2 (2) (2017) 454–461.
[8] R. Pärnamäe, et al., Bipolar membranes: A review on principles, latest developments, and applications, J. Memb. Sci. 617 (2021), 118538.
[9] M.D. Eisaman, Negative Emissions Technologies: The Tradeoffs of Air-Capture Economics, Joule 4 (3) (2020) 516–520.
[10] M.D. Eisaman, J.L.B. Rivest, S.D. Karnitz, C.-F. de Lannoy, A. Jose, R.W. DeVaul, K. Hannun, Indirect ocean capture of atmospheric CO2: Part II. Understanding the cost of negative emissions, Int. J. Greenh. Gas Control 70 (2018) 254–261.
[11] N. Prihasto, Q.-F. Liu, S.-H. Kim, Pre-treatment strategies for seawater desalination by reverse osmosis system, Desalination 249 (1) (2009) 308–316.
[12] C. Bjg, K. Pillai, "Calcium Carbonate MARKET ANALYSIS (2016–2027", 2019.).
[13] C.M. Woodall, N. McQueen, H. Pilorgé, J. Wilcox, Utilization of mineral carbonation products: current state and potential, Greenh. Gases Sci. Technol. 9 (6) (Dec. 2019) 1096–1113.
[14] J. van Heek, K. Arning, M. Ziefle, Reduce, reuse, recycle: Acceptance of CO2-utilization for plastic products, Energy Policy 105 (2017) 53–66.
[15] R. Chang, S. Kim, S. Lee, S. Choi, M. Kim, Y. Park, Calcium Carbonate Precipitation for CO2 Storage and Utilization: A Review of the Carbonate Crystallization and Polymorphism, Front. Energy Res. 5 (2017) 17.
[16] Y. Zhao, J. Wang, Z. Ji, J. Liu, X. Guo, J. Yuan, A novel technology of carbon dioxide adsorption and mineralization via seawater decalcification by bipolar membrane electrodialysis system with a crystallizer, Chem. Eng. J. 381 (8) (2020), 122542.
[17] E.C. La Plante, et al., Saline Water-Based Mineralization Pathway for Gigatonne-Scale CO2Management, ACS Sustain. Chem. Eng. 9 (3) (2021) 1073–1089.
[18] S. Datta, et al., Electrochemical CO_2 Capture Using Resin-Wafer Electrodeionization, Ind. Eng. Chem. Res. 52 (43) (2013) 15177–15186.
[19] R.E. Zeebe, D. Wolf-Gladrow, CO2 in seawater: equilibrium, kinetics, isotopes, no. 65, Gulf Professional Publishing, 2001.
[20] A. G. Dickson, "The carbon dioxide system in sea water: equilibrium chemistry and measurements," *Guid. Best Pract. Ocean Acidif. Res. Data Report.*, no. January 2010, p. 260 p., 2010.
[21] J.N. Butler, Carbon dioxide equilibria and their applications, CRC Press, 1991.
[22] V.L. Snoeyink, D. Jenkins, Water chemistry, John Wiley & Sons Ltd (1980).
[23] S. Emerson, J. Hedges, Chemical oceanography and the marine carbon cycle, Cambridge University Press, 2008.
[24] J.-H. Bang, S.C. Chae, S.-W. Lee, J.-W. Kim, K. Song, J. Kim, W. Kim, Sequential carbonate mineralization of desalination brine for CO2 emission reduction, J. CO2 Util. 33 (2019) 427–433.
[25] M.J. Mitchell, O.E. Jensen, K.A. Cliffe, M.M. Maroto-Valer, A model of carbon dioxide dissolution and mineral carbonation kinetics, Proc. R. Soc. A Math. Phys. Eng. Sci. 466 (2117) (2010) 1265–1290.
[26] Y. Lei, B. Song, R.D. van der Weijden, M. Saakes, C.J.N. Buisman, Electrochemical Induced Calcium Phosphate Precipitation: Importance of Local pH, Environ. Sci. Technol. 51 (19) (Oct. 2017) 11156–11164.
[27] L. Boels, R.M. Wagterveld, M.J. Mayer, G.J. Witkamp, Seeded calcite sonocrystallization, J. Cryst. Growth 312 (7) (2010) 961–966.
[28] A. Banerjee, Estimation of dolomite formation: Dolomite precipitation and dolomitization, J. Geol. Soc. India 87 (5) (2016) 561–572.
[29] L.V. Zaitseva, V.K. Orleanskii, L.M. Gerasimenko, G.T. Ushatinskaya, The role of cyanobacteria in crystallization of magnesium calcites, Paleontol. J. 40 (2) (2006) 125–133.
[30] B. Kutus, A. Gácsi, A. Pallagi, I. Pálinkó, G. Peintler, P. Sipos, A comprehensive study on the dominant formation of the dissolved Ca(OH)2(aq) in strongly alkaline solutions saturated by Ca(ii), RSC Adv. 6 (51) (2016) 45231–45240.
[31] R. Sharifian, M.A. Blommaert, M. Bremer, R.M. Wagterveld, D.A. Vermaas, Intrinsic bipolar membrane characteristics dominate the effects of flow orientation and external pH-profile on the membrane voltage, J. Memb. Sci. (2021), 119686.
[32] J.C. Bui, I. Digdaya, C. Xiang, A.T. Bell, A.Z. Weber, Understanding Multi-Ion Transport Mechanisms in Bipolar Membranes, ACS Appl. Mater. Interfaces 12 (47) (Nov. 2020) 52509–52526.
[33] M.A. Blommaert, D. Aili, R.A. Tufa, Q. Li, W.A. Smith, D.A. Vermaas, Insights and Challenges for Applying Bipolar Membranes in Advanced Electrochemical Energy Systems, ACS Energy Lett. 6 (7) (Jul. 2021) 2539–2548.
[34] R.A. Berner, J.T. Westrich, R. Graber, J. Smith, C.S. Martens, Inhibition of aragonite precipitation from supersaturated seawater; a laboratory and field study, Am. J. Sci. 278 (6) (1978) 816–837.
[35] D. Buhmann, W. Dreybrodt, Calcite dissolution kinetics in the system of water-carbon dioxide-calcium carbonate with participation of foreign ions, Chem. Geol. 64 (1) (1987) 89–102.
[36] G. Falini, S. Fermani, G. Tosi, E. Dinelli, Calcium Carbonate Morphology and Structure in the Presence of Seawater Ions and Humic Acids, Cryst. Growth Des. 9 (5) (May 2009) 2065–2072.
[37] N. Spanos, P.G. Koutsoukos, Kinetics of Precipitation of Calcium Carbonate in Alkaline pH at Constant Supersaturation. Spontaneous and Seeded Growth, J. Phys. Chem. B 102 (34) (Aug. 1998) 6679–6684.
[38] H. Teng, S.M. Masutani, C.M. Kinoshita, G.C. Nihous, Solubility of CO2 in the ocean and its effect on CO2 dissolution, Energy Convers. Manag. 37 (6–8) (1996) 1029–1038.
[39] S. Zhong, A. Mucci, Calcite precipitation in seawatre using a constant addtion technique, Geochim. Cosmochim. Acta 57 (1993) 1409–1417.
[40] D.A. Vermaas, S. Wiegman, T. Nagaki, W.A. Smith, Ion transport mechanisms in bipolar membranes for (photo)electrochemical water splitting, Sustain. Energy Fuels 2 (9) (2018) 2006–2015.
[41] I. Zaslavschi, H. Shemer, D. Hasson, R. Semiat, Electrochemical CaCO3 scale removal with a bipolar membrane system, J. Memb. Sci. 445 (2013) 88–95.
[42] W. Sun, S. Jayaraman, W. Chen, K. A. Persson, and G. Ceder, "Correction: Nucleation of metastable aragonite CaCO3in seawater (Proceedings of the National Academy of Sciences of the United States of America (2015), 112:3199-3204 (DOI: 10.1073/pnas.1423898112))," *Proc. Natl. Acad. Sci. U. S. A.*, vol. 112, no. 20, p. E2735, 2015.
[43] K.J. Davis, P.M. Dove, J.J. De Yoreo, The role of Mg2+ as an impurity in calcite growth, Science (80-.) 290 (5494) (2000) 1134–1137.

[44] T. Østvold, P. Randhol, Kinetics of CaCO3 scale formation. The influence of temperature, supersaturation and ionic composition. in *International Symposium on Oilfield Scale*, 2001.
[45] K.J. Davis, P.M. Dove, L.E. Wasylenki, J.J. De Yoreo, Morphological consequences of differential Mg2+ incorporation at structurally distinct steps on calcite, Am. Mineral. 89 (5-6) (2004) 714–720.
[46] V. De Choudens-Sanchez, L.A. Gonzalez, Calcite and aragonite precipitation under controlled instantaneous supersaturation: elucidating the role of CaCO3 saturation state and Mg/Ca ratio on calcium carbonate polymorphism, J. Sediment. Res. 79 (6) (2009) 363–376.